



Consequences of large strain anisotropic work-hardening in cold forging

Felix Kolpak¹ · Oliver Hering¹ · A. Erman Tekkaya¹

Received: 21 June 2021 / Accepted: 17 August 2021 / Published online: 21 October 2021
© The Author(s) 2021

Abstract

The influence of anisotropic work-hardening on the component properties and process forces in cold forging is investigated. The focus is on the material behaviour exhibited after strain path reversals. The work-hardening of three steels is characterized for large monotonic strains (equivalent strains up to 1.7) and subsequent strain path reversals (accumulated strains up to 2.5). Tensile tests on specimens extracted from rods forward extruded at room temperature reveal an almost linear work-hardening for all investigated steels. The application of compressive tests on extruded material gives insights into the non-monotonic work-hardening behaviour. All previously reported anisotropic work-hardening phenomena such as the Bauschinger effect, work-hardening stagnation and permanent softening are present for all investigated steels and intensify with the pre-strain. Experimental results of 16MnCrS5 were utilized to select constitutive models of increasing complexity regarding their capability to capture anisotropic work-hardening. The best fit between experimental and numerical data was obtained by implementation of a modified Yoshida-Uemori model, which is able to capture all observed anisotropic work-hardening phenomena. The constitutive models were applied in simulations of single- and multi-stage cold forming processes, revealing the significant effect of anisotropic hardening on the predicted component properties and process forces, originating in the process-intrinsic strain path reversals as well as in strain path reversals between subsequent forming stages. Selected results were validated experimentally.

Keywords Flow curve · Forward rod extrusion · Bauschinger effect

Introduction

The goals of metal forming process design have long exceeded the mere shaping of parts. Property changes of cold forged parts due to plastic deformations have received increasing attention in the last years including the mechanical properties [1] and damage [2]. An exact incorporation of the material behaviour under complex strain paths is necessary to predict and exploit these property changes by numerical simulations. Previous research works have rarely considered anisotropic hardening in the field of cold bulk forming preventing an accurate prediction of a formed components properties and its performance. In the scope of this paper, the phrase “anisotropic work-hardening” refers to the deviation of a metal’s yield surface from an initially isotropic state,

captured for example by the concept of combined isotropic-kinematic hardening.

Bauschinger [3] found, that when a material is plastically deformed under tension and then compressed, the yield stress under reverse loading ($\sigma_{f,reverse}$) is lower than the flow stress before unloading ($\sigma_{f,forward}$) (Fig. 1).

Consequently, the common assumption of isotropic hardening is inaccurate, whenever a region of material undergoes a strain path reversal.

In addition to the Bauschinger effect, which describes only the difference of the flow stress in tensile and compressive direction, materials can exhibit additional anisotropic work-hardening phenomena. The illustrated effects (see Fig. 1) include the smooth transition from the elastic into the elastic-plastic state immediately after a strain path reversal, referred to as transient hardening, work-hardening stagnation and permanent softening. Masing [4] explained the Bauschinger effect with differences in the orientation of individual crystals within a polycrystal, leading to differences in the yield strength of individual crystals in different directions. Orowan [5] proposed that the Bauschinger effect is connected to the

✉ Felix Kolpak
felix.kolpak@iul.tu-dortmund.de

¹ Institute of Forming Technology and Lightweight Components (IUL), TU Dortmund University, 44227 Dortmund, Germany

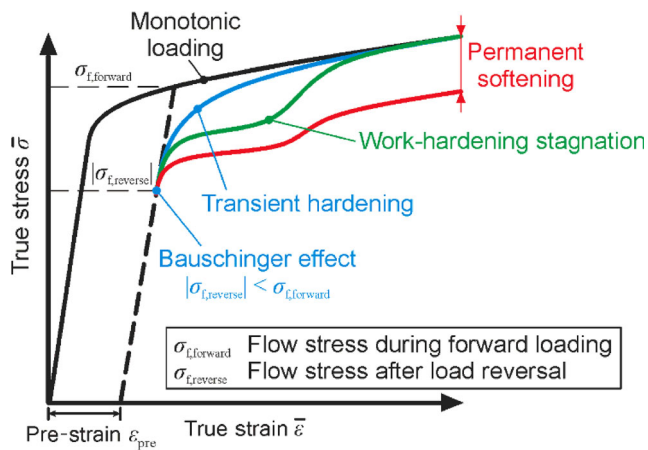


Fig. 1 Anisotropic work-hardening phenomena observed after strain path reversal and comparison with monotonic loading

interaction of dislocations with obstacles. Such obstacles can be clusters of interstitial atoms of a secondary phase. During forward loading, the obstacles must be sliced or bypassed, during which so-called elastic back stresses are generated, which add up to the total stress during reverse loading. Sliced obstacle lead to an eased dislocation motion upon load reversal. Sleswyk et al. [6] explained the Bauschinger effect and the accompanying transient hardening by a “loss of strain” after reloading, based on a decrease of dislocation density. Sillekens et al. [7] explained the lowered flow curve with the unpinning of dislocation structures that do not encounter new obstacles during the reverse motion. Hasegawa et al. [8] found that the stagnation of the work-hardening curve after a load reversal is related to the accompanying disintegration of cell walls, while simultaneously new dislocations are generated. Work-hardening resumes after all remaining cell walls from the previous loading have dissolved. For single crystal zinc specimens Edwards and Washburn [9] observed, that the stress during reverse loading is permanently lower than the flow stress under monotonic loading. The authors reported that the “permanently lost strain” increases linearly with the pre-strain and explained this with the annihilation of dislocations trapped in the crystal during forward loading. Sillekens et al. [7] attributed the linear correlation between the pre-strain and the magnitude of permanent softening of Ck45 steel to the gradually obstacle-free slip-planes in the reverse dislocation moving direction.

Many authors identified the pre-strain as the most important factor influencing the intensity of anisotropic hardening effects. Sowerby et al. [10] observed for three steel grades that the intensity of permanent softening correlates with the pre-strain. Scholtes et al. [11] reported for normalized Ck45 steel that the Bauschinger coefficient saturates with increasing pre-strains and the intensity of permanent softening increases without any signs of stagnation. Sillekens et al. [7] conducted similar tests on C45 steel and found a linear correlation

between the pre-strain and permanent softening. Yoshida et al. [12] performed forward-reverse tensile tests reporting 2.5% permanent softening for mild steel sheets and up to 7.5% for an advanced high strength steel.

In sheet metal forming anisotropic hardening effects receive frequent attention, as spring back, a major concern in this research field, is highly affected by non-proportional strain paths and the accompanying work-hardening phenomena. This becomes especially important when large regions are bent and unbent multiple times, e.g. in deep drawing with draw beads. Ghaei and Green [13] showed by the example of the NUMISHEET 2005 benchmark that the accuracy of spring back simulations can be increased drastically utilizing a mixed isotropic-kinematic hardening model. A comprehensive review on the influence of anisotropic hardening on spring back was given by Wagoner et al. [14]. The most common method to characterize materials in the field of sheet metal forming is the tension-compression test [15] (Fig. 2a). Due to the low bending stiffness of the slender specimens, the achievable tensile pre-strains are highly limited [16]. As a countermeasure Kuwabara et al. [17] introduced a support device, while Boger [18] used on special specimen geometries. Other characterization methods include the cyclic planar shear test [19], the cyclic bending test [20] and the cyclic in-plane torsion test [21].

In the literature, experimental results on the influence of anisotropic hardening in bulk forming processes are rare and focus mainly on the application of pre-drawn wire in subsequent forming processes. Tozawa and Kojima [22] conducted cold heading tests on different pre-drawn steels and showed that the flow curve and formability depends on the die angle in the wire drawing process, in which the material is pre-strained under tension. Havranek [23] showed that pre-drawing leads the two investigated steels AISI K1020 and AISI K1040 to exhibit work-hardening stagnation and permanent softening during subsequent cold heading. This leads the forming work required for compression to be even lower than that of spheroidized material. Ma [24] showed that a consideration of the Bauschinger effect in cold heading simulations can improve the quality of geometry prediction. Miki and Toda [25] investigated the influence of work-hardening in drawing and subsequent upsetting and subsequent forward rod extrusion. They found, that the anisotropic hardening only affects the first process sequence which corresponds to a tension-compression strain path change, emphasizing that anisotropic hardening must be considered for an accurate prediction of tool life. Galdos et al. [26] investigated the influence of strain path reversals in the production of ball pins. They modelled the workpiece behavior by means of the Chaboche hardening model (1986) and observed that the geometry, residual stress and process forces are only weakly affected by the Bauschinger effect as most material regions do not undergo strain path changes.

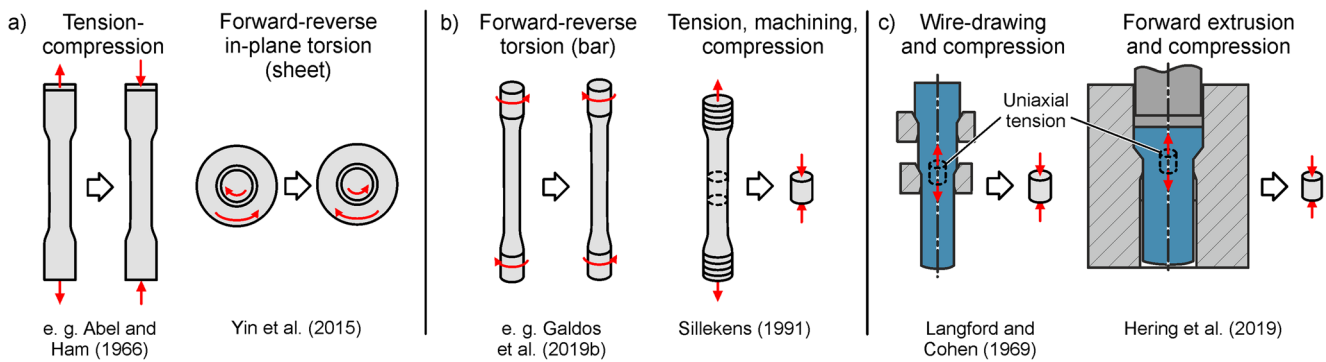


Fig. 2 Selected methods to characterize the anisotropic hardening behaviour during strain path reversals in (a) sheet metal forming and (b) bulk metal forming; (c) Application of forming technologies to generate pre-strained specimens for subsequent mechanical testing

In bulk metal forming, the material is typically available in form of bars or slabs. Analogously to the characterization of sheet specimens, a common method to characterize material in the form of bars is the tension-compression test of round specimens. Due to the high length to diameter ratio and thus the low bending stiffness, standardized tensile specimens according to the international standard ISO 6892-1 are not suited to apply strain path reversals. Scholtes et al. [11] tested different types of specimen geometries and test apparatuses to overcome this limitation. Despite these precautions, the achieved plastic pre-strains were limited to 3.7% due to the restricted material flow at the specimen's end faces, introducing an unknown stress distribution. Galdos et al. [27] investigated the load reversal behavior of 42CrMoS4Al case-hardening steel by means of cyclic torsion tests on cylindrical specimens (Fig. 2b). They were able to characterize the material to equivalent pre-strains of $\varepsilon_{\text{pre}} = 0.7$ and observed the Bauschinger effect, transient hardening, work-hardening stagnation and permanent softening. Sillekens et al. [28] conducted upsetting tests on cylindrical specimens machined from previously elongated C22 steel and CuZn37 bars and were able to achieve pre-strains of $\varepsilon_{\text{pre}} > 0.3$, showing that the flow stress and hardening rate in reverse direction drops significantly with increasing pre-strain.

To overcome the limits of conventional characterization procedures and reach larger strains ($\varepsilon > 1$), some authors utilized different forming technologies to generate pre-strained specimens for subsequent mechanical testing (Fig. 2c). Langford and Cohen [29] conducted upsetting tests on drawn iron wires with large pre-strains of $\varepsilon_{\text{pre}} = 4.5$, demonstrating that the material exhibits extensive softening after the strain path reversal. Pöhlandt [30] performed upsetting tests on cold-extruded QSt32–3 to obtain large strain flow curves and observed an “abnormal” hardening slope, which Doege et al. [31] attributed to the strain path reversal between extrusion and upsetting. Nehl [32] investigated the influence of the extrusion strain in forward rod extrusion on the flow stress in subsequent compression for four types of machining steels and found that even at the lowest investigated pre-strain of $\varepsilon_{\text{pre}} = 0.5$ all materials exhibit softening in subsequent upsetting.

In the field of cold forging, up to now, the consequences of anisotropic hardening have been rarely considered in terms of numerical simulations. To model strain path reversal related work-hardening phenomena kinematic or distortional hardening models can be applied, e. g. as described by Chaboche [33] or Barlat et al. [34], respectively. So far, such enhanced models have been rarely applied in the field of cold bulk forming simulations, partly due to the missing experimental characterization procedures necessary to fit the model parameters and partly due to the model's limitations to correctly capture anisotropic hardening at the large strains occurring in cold bulk forming processes. Suh et al. [35] applied a simple kinematic hardening model in simulations of forward extrusion simulations and observed that the residual stresses are highly affected. Narita et al. [36] compared different process sequences for the production of cold forged bolts, utilizing the advanced Yoshida et al. [12] hardening model in their simulations. By modelling the Bauschinger effect in the simulation, they were able to improve the prediction accuracy of the part's strength.

Considering the role of work-hardening for the product and process properties in metal forming processes, the lack of knowledge on the anisotropic work-hardening behavior over the complete strain regime leads to significant uncertainties in the results of cold forging simulations, making impossible an accurate prediction of product properties and process forces. The goal of this work is to quantify and model the influence of anisotropic work-hardening on process forces and component properties in cold forging with a focus on strain path reversals. The methodology includes the following stages:

- 1) Establishment of experimental methods to characterize the large strain anisotropic work-hardening behaviour of cold forging steels over the whole relevant pre-strain regime and comparison of materials,
- 2) assessment and modification of constitutive models to capture all observed anisotropic work-hardening phenomena exhibited after strain path reversal considering large equivalent strains and pre-strains > 1 ,
- 3) application and comparison of isotropic and anisotropic work-hardening models in cold forging simulations,

Table 1 Chemical composition of investigated steels (vol-%)

Steel	C	Si	Mn	P	S	Cr	Mo
16MnCr5 (1.7139)	0.152	0.172	1.194	0.013	0.027	1.040	0.042
C15 (1.0401)	0.153	0.231	0.570	0.123	0.018	0.093	0.036
100Cr6 (1.3505)	0.967	0.178	0.351	0.009	0.017	1.478	0.019

- 4) determination of the influence of anisotropic hardening on the process forces and component properties in single- and multi-stage cold forging processes.

To allow the assessment of the constitutive models with regard to their prediction accuracy, selected results are validated experimentally.

Characterization of large strain anisotropic work-hardening

In the following, the materials and methods used to characterize the work-hardening behaviour after strain path reversals at large strains are presented.

Materials

Table 1 shows the chemical compositions of the three investigated steels. The steels were selected according to their negligible initial tension-compression asymmetry as well as to cover a range of anisotropic work-hardening behaviours.

Methods

Various characterization methods were applied and compared to capture the work-hardening behaviour over different strain and pre-strain regimes (Fig. 3). For small strains ($0 < \bar{\varepsilon} < 0.5$) conventional tensile and upsetting tests were conducted. Tensile tests on cold extruded material were applied to capture the large strain work-hardening behaviour as suggested by

Hering et al. [37] ($0.5 < \bar{\varepsilon} < 1.7$). Tensile test specimens are extracted from the center of forward extruded bars which contain a uniformly formed region in the core, in which the equivalent strain can be calculated analytically as

$$\varepsilon_{\text{ex}} = 2 \cdot \ln \left(\frac{d_0}{d_1} \right). \quad (1)$$

Herein, d_0 and d_1 are the diameter of the extrudate before and after forward extrusion, respectively. The forward extrusion setup to produce specimens with various extrusion strains is described in detail in Hering et al. [37].

By performing tensile tests on the extrudates with different extrusion strains, individual points of a large strain flow curve are obtained under an overall monotonic strain path as the deviatoric stress state in the forming zone of forward extrusion equals that of a uniaxial tensile test. The equivalent strain in the extracted specimens is higher than the nominal extrusion strain, as the material is additionally sheared toward the surface and must thus be determined numerically.

To characterize the work-hardening behaviour subsequent to a strain path reversal, upsetting tests were conducted on material pre-strained by tensile tests (small pre-strains) and pre-strained by forward rod extrusion (large pre-strains). The specimen geometries are shown in Fig. 4.

The tensile and upsetting tests were performed on a Zwick Roell Z250 universal testing machine. Tensile tests were performed at room temperature according to DIN EN ISO 6892-1 with a constant strain rate of 0.0067 s^{-1} . The specimen elongation was measured with a macro-extensometer with a gauge length of 40 mm. The upsetting tests were conducted according to DIN 50106 at room temperature with a constant strain rate of 0.0067 s^{-1} . In order to reduce the friction, the end faces of the cylindrical specimens were lubricated with Teflon spray. The specimen height was measured indirectly in terms of the cross-head travel, which was corrected for the elastic deflection of the test machinery under compressive loading. The stress-strain curves obtained under compression were corrected for friction by the method explained by Siebel [38]. According to Hering et al. [37] the friction coefficient was assumed as $\mu = 0.05$. All

Fig. 3 Experimental procedures to determine the (a) large strain monotonic and (b) non-monotonic work-hardening behaviour

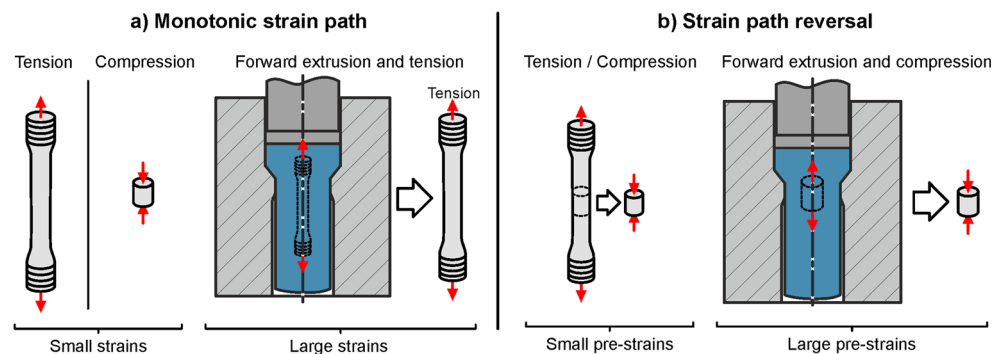
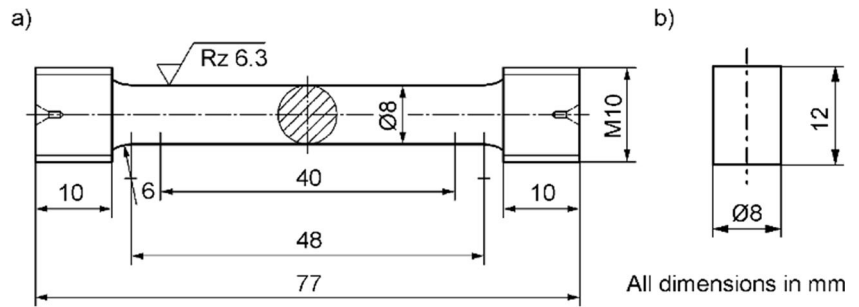


Fig. 4 Specimen geometries for (a) tensile test, (b) upsetting test



flow stress values presented in the following correspond to the mean of least four individual measurements.

Large strain monotonic work-hardening behaviour

The results of the tensile tests and upsetting tests on 16MnCrS5 specimens and the data obtained by tensile tests on forward extruded material is shown in Fig. 5.

In the case of the tensile test, the maximum achieved strain ($\bar{\epsilon} = 0.14$) was limited by the occurrence of necking, in upsetting by barrelling ($\bar{\epsilon} = 0.5$) and in forward extrusion by the highest possible extrusion strain $\epsilon_{ex} = 1.5$ (corresponding to an effective strain in the specimen of $\bar{\epsilon} = 1.68$), which is limited by the strength of the extrusion tools. The data from the tensile tests on the as-received material and the tensile tests on forward extruded material were combined to generate large strain flow curves. It is noted that the pre-strained tensile specimens start necking almost immediately after plastic flow sets in. The data in between two flow stress points obtained by tensile tests on forward extruded material is interpolated linearly. All three methods show a high correlation as reported in Hering et al. [37].

The large strain flow curves of the investigated steels obtained by tensile tests and tensile tests on cold extruded material are shown in Fig. 6.

After an initially steep flow curve increase, all materials transition into near linear work-hardening, as opposed to the

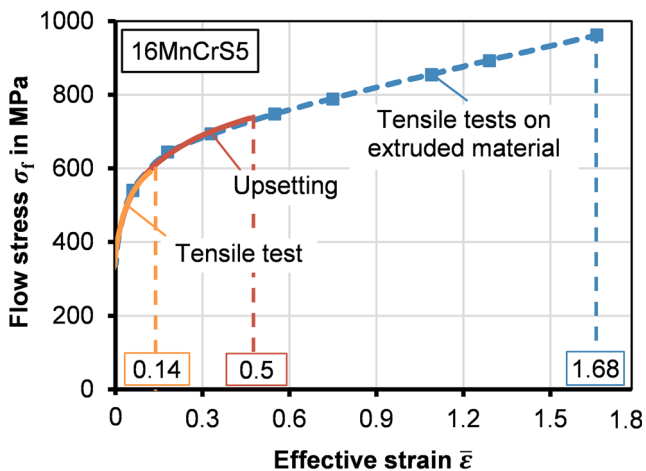


Fig. 5 Comparison of methods to obtain the monotonic work-hardening behaviour of the case-hardening steel 16MnCrS5

commonly assumed saturating behaviour. The observed linear hardening at large strains is characteristic for the fibrous microstructure evolving under uniaxial tension and the corresponding mode of deformation.

Large strain work-hardening behaviour after strain path reversal

The results of tensile and upsetting tests on forward extruded material are shown in Fig. 7. As the subsequent upsetting after forward extrusion corresponds to a full strain path reversal, the flow curves under compression include all work-hardening phenomena presented in Fig. 1. All curves obtained by upsetting tests (red lines) are significantly lower than the corresponding stress-envelope curves (dashed blue lines) generated by the tensile stress. The steels exhibit the classical Bauschinger effect, in terms of flow stress difference between monotonic loading and after strain path reversal, transient hardening, work-hardening stagnation and permanent softening. The intensity of all these effects increases with the pre-strain ϵ_{pre} . While 16MnCrS5 maintains its work-hardening rate after subsequent compression, the work-hardening rate of 100Cr6 and C15 is altered permanently. In the cases of C15 and 100Cr6, the work-hardening rate under subsequent compression does not seem to revert to the work-hardening rate under monotonic loading. In the extreme case of C15 the work-hardening potential seems to vanish completely for $\epsilon_{pre} > 0.7$.

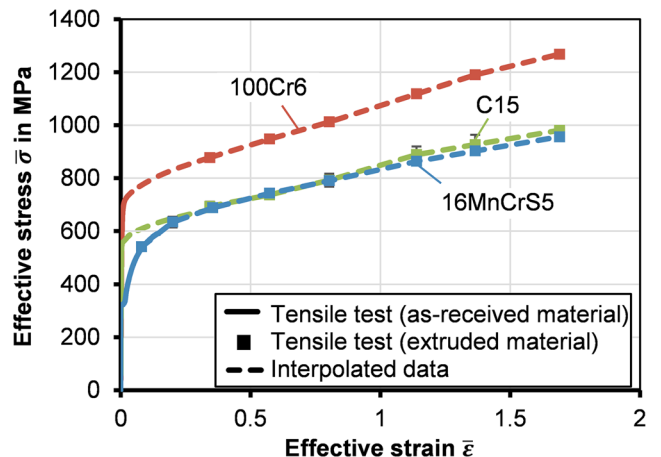


Fig. 6 Large strain monotonic flow curves of different steels

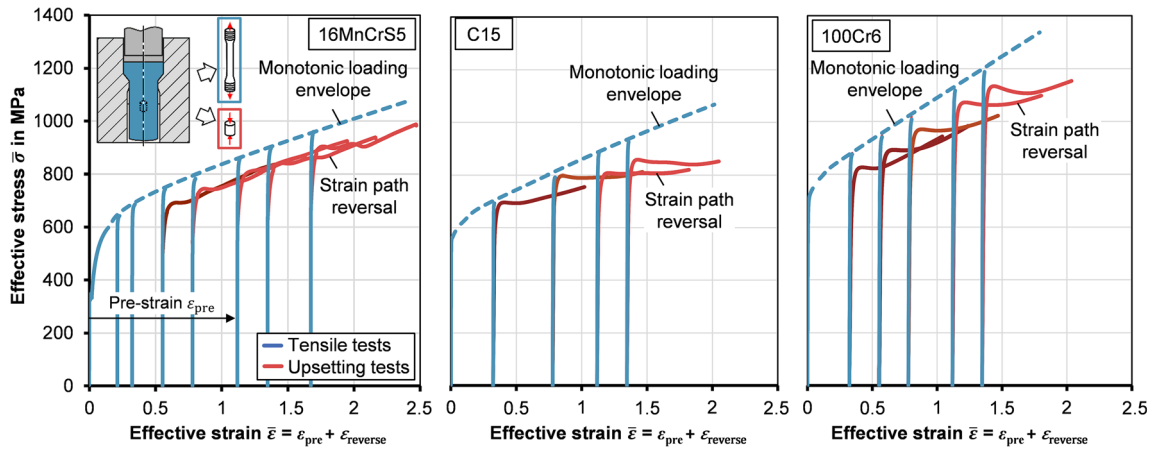


Fig. 7 Stress-strain behaviour of various materials determined by tensile and upsetting tests subsequent to forward rod extrusion

In order to quantify the anisotropic work-hardening phenomena, the definitions according to Fig. 8 are used.

The Bauschinger coefficient χ is defined as:

$$\chi(\epsilon_{pre}) = \left| \frac{\sigma_{f,reverse}}{\sigma_{f,forward}} \right|. \tag{2}$$

Herein, $\sigma_{f,forward}$ and $\sigma_{f,reverse}$ are the flow stress before and after the strain path reversal, respectively. As the flow stress of pre-strained materials cannot be identified easily, due to the smooth transition from the elastic into the elastic-plastic regime, the flow stress was approximated by the proof stress at 0.2% plastic strain ($R_{p0.2\%}$).

The intensity of transient hardening and work-hardening stagnation cannot be captured by a scalar value, thus they are quantified by means of the normalized stress difference curve

$$\Delta\sigma_f(\epsilon_{max}, \epsilon_{pre}) = \frac{(\sigma_{f,forward}(\epsilon_{max}) - |\sigma_{f,reverse}(\epsilon_{max}, \epsilon_{pre})|)}{\sigma_{f,forward}(\epsilon_{max})}. \tag{3}$$

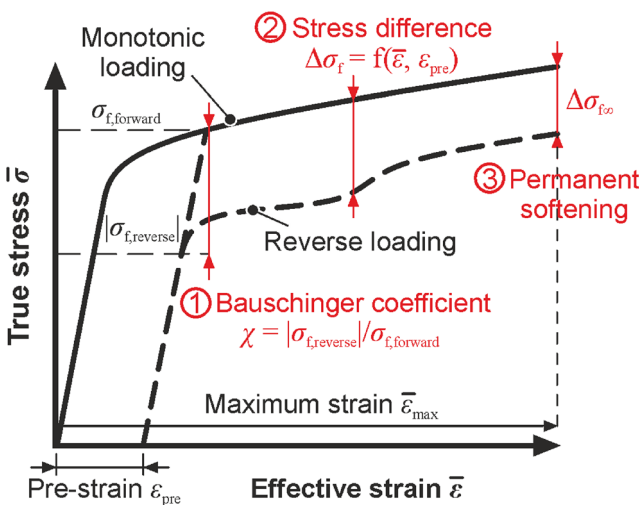


Fig. 8 Definition of strain path reversal effects

Permanent softening $\Delta\sigma_{f,so}$ is defined by the difference between the last measured points of each flow curve at ϵ_{max} obtained for subsequent compression and the flow stress under monotonic loading at the same effective strain. As the flow curves for monotonic tension and subsequent compression do not necessarily become parallel (e. g. in the cases of C15 and 100Cr6) $\Delta\sigma_{f,so}$ represents only an approximation of permanent softening, as the continuation of the curves at large reverse strains remains unknown. The influence of the pre-strain on the Bauschinger coefficient of the three steels is plotted in Fig. 9. The curves in the dashed box correspond to data obtained by upsetting tests on material pre-strained by uniaxial tension. In this small pre-strain regime, the Bauschinger coefficients show the frequently reported steep drop with a fast saturation toward constant values in the range of $0.66 < \chi < 0.71$.

The curves in the dashed box correspond to data obtained by upsetting tests on material pre-strained by uniaxial tension. In this small pre-strain regime, the Bauschinger coefficients show the frequently reported steep drop with a fast saturation

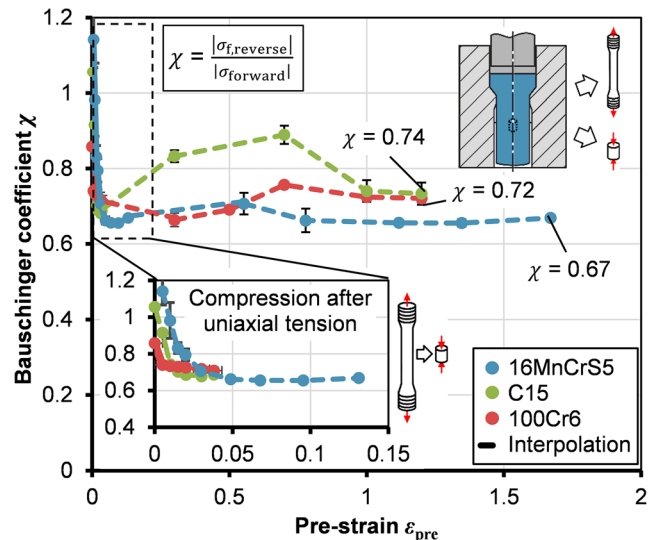


Fig. 9 Influence of the pre-strain on the Bauschinger coefficient

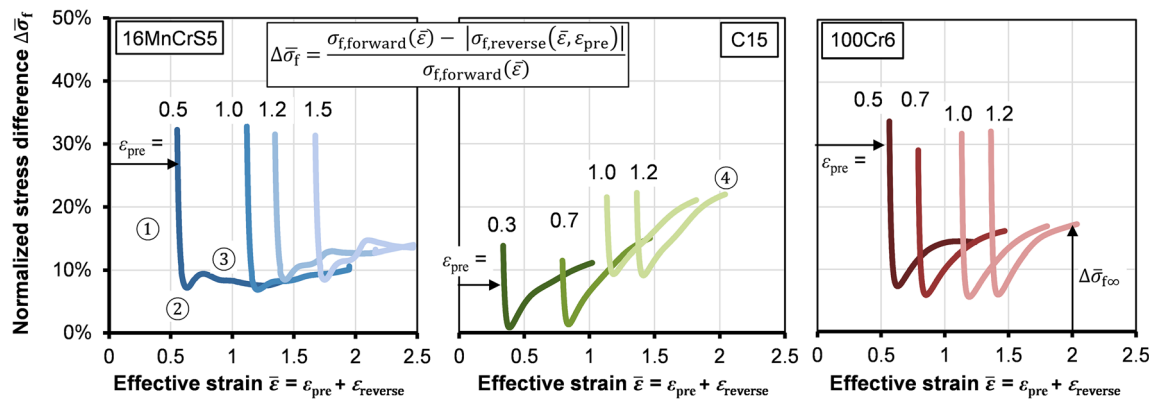


Fig. 10 Stress difference curves calculated according to the definition given by Eq. 5

toward constant values in the range of $0.66 < \chi < 0.71$. At larger pre-strains, all steels show an initial increase of the Bauschinger coefficients, before falling back and saturating in the range of $0.67 < \chi < 0.74$.

The stress difference curves according to the definition given in Eq. 3 are plotted in Fig. 10. The beginning of each curve marks the initial flow stress difference after the strain path reversal as quantified by the Bauschinger coefficient.

The curves then traverse into a steep drop ①, followed by another increase ②. This oscillating behaviour highlights the region of work-hardening stagnation. For 16MnCrS5 the curves flatten at increasing total strains, indicating that the work-hardening slope before and after the strain path reversal are equal ③. This is not the case for C15 and 100Cr6, as the slope for subsequent compression remains lower than the slope under monotonic tension ④.

The last point of each stress difference curve marks the normalized permanent softening (Fig. 11). For all steels permanent softening increases with the pre-strain and is most pronounced for C15, which loses more than 22% of its work-hardening potential due to the strain path reversal.

In the application of the steels in cold forming processes with strain path reversals, this permanent loss of work-hardening is expected to translate directly into a decrease of the forming forces.

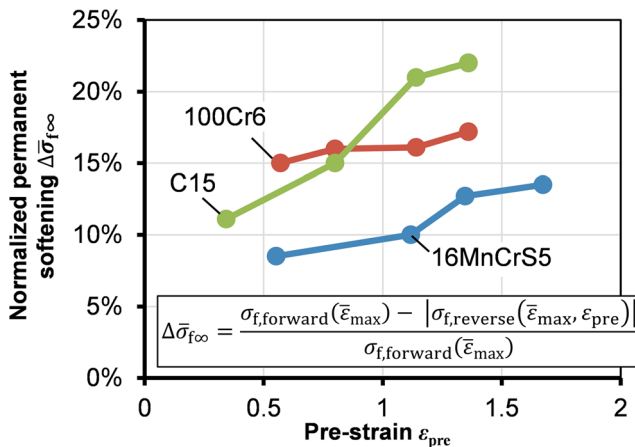


Fig. 11 Influence of pre-strain on normalized permanent softening

In summary, the applied experimental methods reveal the monotonic work-hardening behaviour of three steels up to large equivalent strains and after strain path reversals with large pre-strains, far exceeding those in the literature (by a factor of more than 5). All investigated steels exhibit significant deviations from the conventionally assumed isotropic hardening behaviour, if the strain path is reversed after previous plastic forward deformation.

Modelling anisotropic work-hardening

Material models and modifications

Based on the characterization results in the previous section, constitutive models of varying complexity were selected and modified with regard to their capabilities to capture the observed anisotropic work-hardening effects:

- a) Isotropic hardening (reference model)
- b) Combined isotropic-kinematic hardening according to Chaboche [33]
- c) Yoshida-Uemori combined hardening [39]

The basic principles of the constitutive models are illustrated in Fig. 12 by means of the corresponding yield surfaces.

In the Chaboche model, the flow stress difference for tension and compression after previous plastic loading is captured by the translation of the yield surface α (back stress), which evolves according to the evolution equations

$$\alpha = \sum_i^n \alpha_i \quad \text{with} \quad d\alpha_i = C_i d\varepsilon^p - \gamma_i \alpha_i d\bar{\varepsilon}, \quad (4)$$

where C_i and γ_i are material parameters and $d\bar{\varepsilon}$ is the effective plastic strain increment. In this paper, a variant of the Chaboche model with two back stress terms ($n = 2$) and $\gamma_2 = 0$ is considered. This setting allows modelling permanent softening as the saturation of the second kinematic hardening term is avoided.

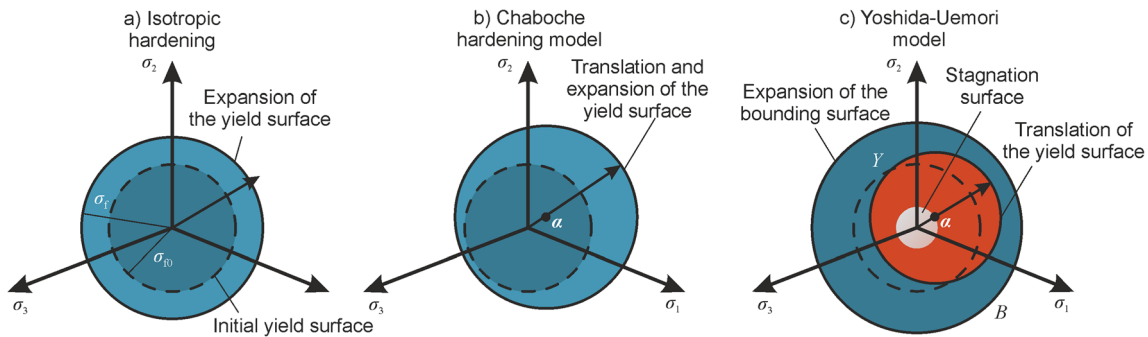


Fig. 12 Basic principal of the investigated constitutive models

The Yoshida and Uemori [39] model is a so-called multi-surface model. The yield surface translates with respect to a bounding surface according to

$$d\theta = c \left[\frac{a}{Y} \eta - \sqrt{\frac{a}{\theta}} \right] d\varepsilon. \tag{5}$$

Here, θ is the position of the yield surface relative to the center of the bounding surface, η is the difference between the stress and the back stress α and $\bar{\theta}$ is the effective value of θ , according to the yield function definition (in the present case, the Von-Mises yield function was used under the assumption of initial isotropy).

The bounding surface translates according to the evolution equation:

$$d\beta = k \left[\frac{b}{Y} \eta - \beta \right] d\varepsilon_{eq}^p. \tag{6}$$

The evolution equation of the yield surface translation (back stress) is given as

$$d\alpha = d\beta + d\theta. \tag{7}$$

In the original formulation of the Yoshida-Uemori model, the isotropic hardening of the bounding surface evolves according to

$$dR = k(R_{sat} - R)d\varepsilon, \tag{8}$$

corresponding to saturating isotropic hardening with a maximum bounding surface radius of R_{sat} . To model the work-hardening stagnation, isotropic hardening of the bounding surface only takes place, if the center of the bounding surface θ lies on the edge of a third surface, the so-called stagnation surface. The evolutions of the stagnation surface translation and expansion are denoted by

$$dq = dq(h) \text{ and} \tag{9}$$

$$dr = dr(h) \tag{10}$$

respectively. The fractions of the two components are controlled by the material parameter h ($0 < h < 1$), which determines the intensity of work-hardening stagnation.

To correctly model the large strain monotonic hardening behaviour observed for 16MnCrS5 the isotropic hardening

component R was generalized as proposed by Yoshida et al. [40] by defining it as a weighted combination of the Swift [41] and Voce [42] hardening laws according to

$$R = wC_{iso}(\varepsilon + \varepsilon_0)^n + (1-w)R_{sat}(1 - e^{-k^*\varepsilon}), \tag{11}$$

with the material parameters, C_{iso} , ε_0 , R_{sat} and k^* and w . In the original model, the rates of expansion and translation of the bounding surface are both controlled by the parameter k ($k = k^*$). In order to increase the flexibility of the Yoshida-Uemori model with regard to the material behaviour at large strains presented in “Characterization of large strain anisotropic work-hardening” section, the parameter k was split into two separate parameters k_1 and k_2 , individually controlling the rate of expansion (Eq. 11, $k^* \rightarrow k_1$) and translation (Eq. 6, $k \rightarrow k_2$) of the bounding surface, respectively. In the following, the model is referred to as the “modified Yoshida-Uemori model”. The material parameters of the modified Yoshida-Uemori model are summarized in Table 2.

The isotropic and combined hardening model according to Chaboche are implemented in Abaqus Standard by default. The Yoshida-Uemori model was implemented by means of a user material subroutine (UMAT) in terms of the semi-implicit integration scheme described by [13]). In this scheme,

Table 2 Material parameters of the modified Yoshida-Uemori model (* new or modified parameters)

Parameter	Description
Yield surface	
Y	Initial yield surface radius
c	Rate of translation
Bounding surface	
B	Initial radius
b	Translation threshold
k_1^*	Rate of expansion
k_2^*	Rate of translation
$w^*, C_{iso}^*, \varepsilon_0^*, n^*, R_{sat}$	Isotropic hardening parameters
Stagnation surface	
h	Intensity of work-hardening stagnation

the plastic strain increments are integrated implicitly, whereas the other state variables are integrated explicitly. To ensure stable convergence, a local sub-stepping algorithm was applied. This is triggered whenever a local plastic strain increment $\Delta\bar{\epsilon}$ exceeds a value of 0.001.

Parameter identification procedure

As all investigated steels exhibit the same anisotropic work-hardening phenomena, differing only in their intensity, 16MnCrS5 was chosen as representative for the numerical investigations. The experimental results of the tensile tests on initial material were used to describe the monotonic work-hardening behaviour in the low strain regime. In the large strain regime, the experimental results from the tensile tests on forward extruded material were utilized. To account for anisotropic hardening the flow curves obtained by upsetting of pre-strained material were considered.

Starting from an initial guess of physically admissible material parameters x_0 , which were based on a preceding parameter sensitivity study, single-element simulations with uniaxial tensile loading are conducted up to the highest experimentally obtained total strain. The results of the uniaxial tensile test simulation are exported at different pre-strains ($\epsilon_{pre,i} = 0.3/0.5/1.0/1.5$) to apply subsequent

strain path reversals. The resulting stress-strain curves of all single-element simulations are exported and compared with the experimental data using the mean square error (MSE). The material parameters are optimized within pre-defined physically admissible parameter ranges, with the goal to minimize the MSE function. The mathematical optimization tool LS-Opt was used to conduct the parameter identification procedure. To find a local minimum of the mean square error function between the experimental and simulated stress-strain curves, the successive response surface method (SRSM) was applied as described in detail by Stander et al. [43]. Abaqus Standard 2019 was used to conduct the single-element simulations. Whenever the mean square error has been reduced in an iteration, the parameter space is scaled down by a factor of 0.6. To prevent overweighting of the stress-strain curves under compression due to the larger total number of data points, the monotonic stress-strain data was weighted with a factor of 2. In the case of isotropic hardening, the experimental data obtained by subsequent compression was discarded.

Parameter identification results

The results of the parameter identification procedure are shown in Fig. 13. For each model, the resulting mean square error is

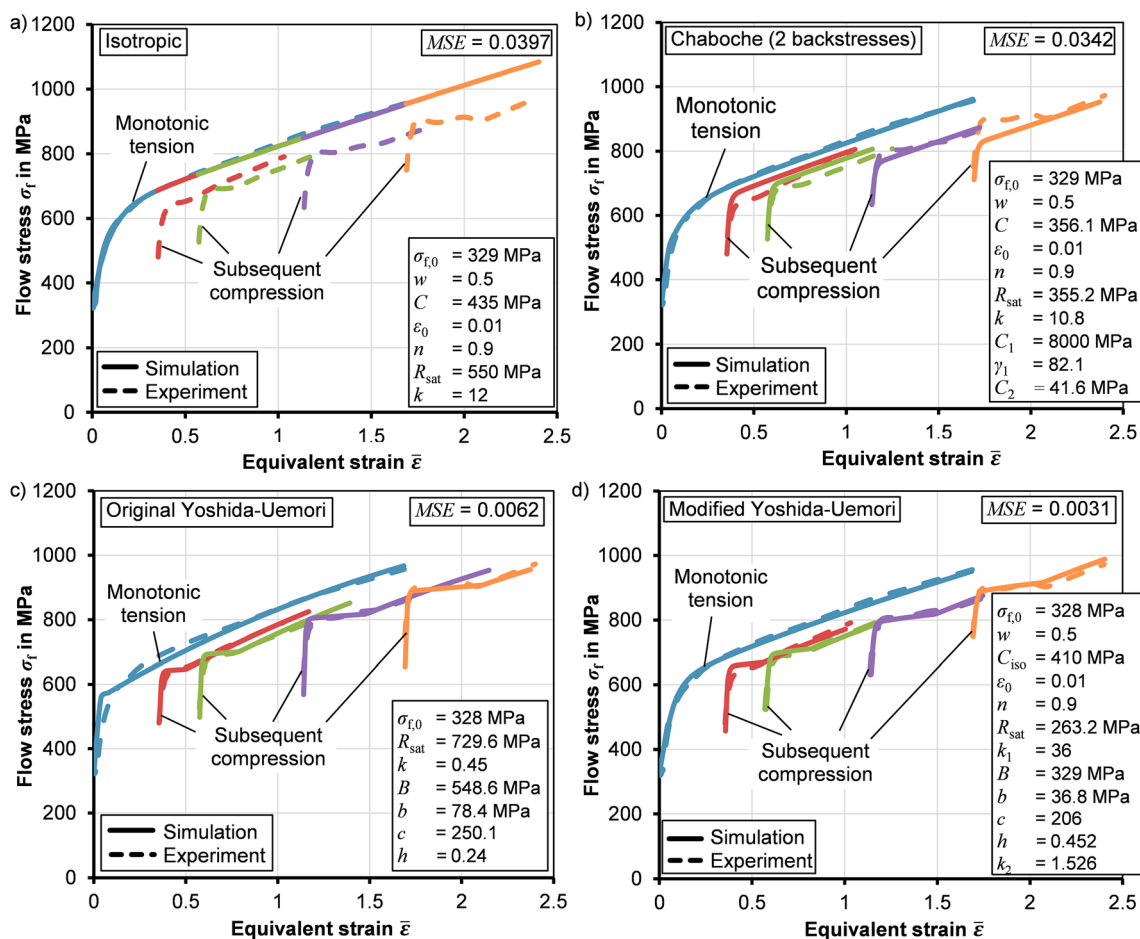


Fig. 13 Comparison of simulated and experimental flow curves of 16MnCrS5 for different constitutive models

given. The material parameters of each investigated constitutive model are given in the boxes. The solid and dashed lines indicate the experimental and numerical flow curves, respectively. All investigated constitutive models capture the monotonic work-hardening behaviour well over the entire investigated strain regime. Consequently, the necessary comparability is given for monotonic strain paths.

As expected, the isotropic hardening model overestimates the flow stress during subsequent compression significantly (Fig. 13a). The Chaboche model (Fig. 13b) is able to capture the classical Bauschinger effect in terms of the lowered flow stress after the load reversal at all investigated pre-strains. The additional non-saturating back stress term even enables modelling of permanent softening. However, its accuracy is limited by the fact that it is controlled only by the single parameter C_2 , which does not yield the flexibility to model to evolution of permanent softening with the pre-strain. Both the original Yoshida-Uemori model (Fig. 13c) and the modified version (Fig. 13d) are able to model all anisotropic hardening phenomena, including the Bauschinger effect, transient hardening, work-hardening stagnation and permanent softening over the complete investigated pre-strain regime. However, the accuracy of the original model, especially in the beginning of monotonic hardening curve, is clearly limited. The modifications of the model, including the generalization of the isotropic hardening of the bounding surface and the parameter split of k into two separate parameters individually controlling the translation and expansion of the boundary surface were necessary to correctly model the monotonic hardening behaviour over the complete investigated monotonic strain regime. This requirement for an accurate prediction of the material behaviour is underlined by the large difference between the optimized values of the new parameters ($k_1 = 36$ and $k_2 = 1.526$).

All constitutive models were applied to describe the material behaviour in cold forging simulations utilizing the optimized material parameters.

Application of large strain work hardening in cold forging

The selected and modified constitutive models presented in the preceding section are applied to cold forging simulations to determine the influence of anisotropic hardening on component properties and process forces.

Investigated cold forging processes

Two basic cold forging processes were analysed in the scope of this paper i. e. forward rod extrusion (Fig. 14a), backward can extrusion (Fig. 14b). The influence of the most important process parameters on the directional flow stress, residual stress and the process forces, including the punch and ejector forces, were evaluated. In addition to the basic cold forging

processes, two multi-stage processes are analysed, which include strain path reversals, i. e. anchor forging, a combination of forward rod extrusion and subsequent upsetting (Fig. 14c) and flange upsetting, a combination of backward can extrusion and upsetting (Fig. 14d). In the case of the multi-stage processes, the influence of anisotropic hardening on the process forces of the second forming stage is investigated.

The process parameters of the four investigated processes are given Table 3. For all processes, the initial workpiece diameter was defined as $d_0 = 30$ mm. Details regarding the setup of the FEM-models are given in Appendix A.1. In the cases of backward can extrusion and multi-stage cold forging, a manual remeshing algorithm was applied to prevent excessive mesh distortion.

Influence of anisotropic hardening on local flow stress

In the case of isotropic hardening, the local flow stress of the formed part is given by the yield condition

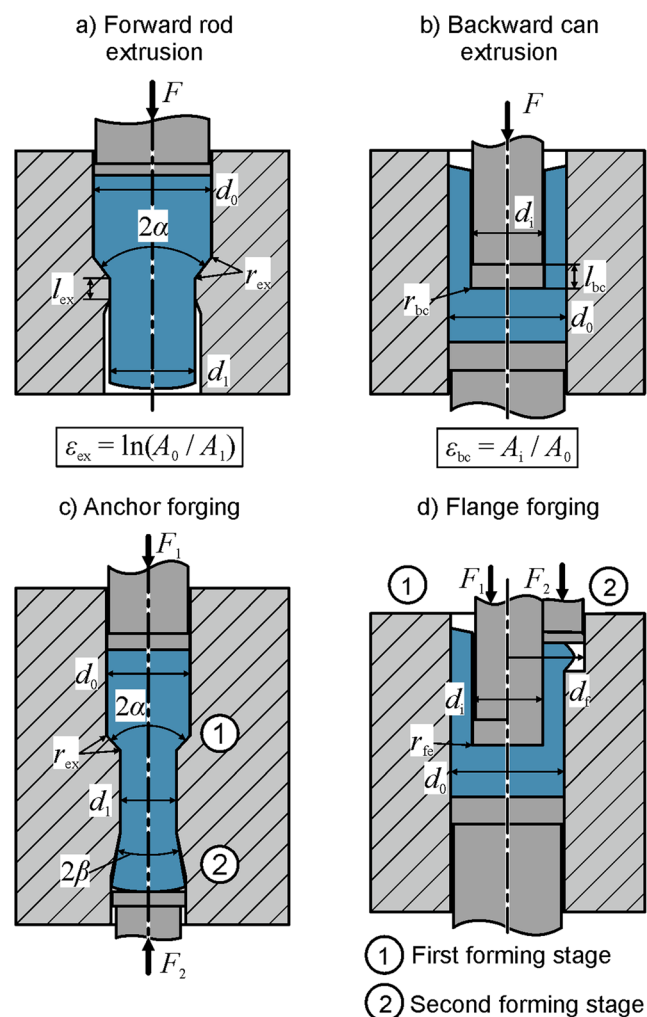


Fig. 14 Investigated cold forging processes

Table 3 Process parameters of the investigated forming processes

Process	Parameter	Symbol	Value
All	Initial diameter	d_0	30 mm
a)	Extrusion strain	ε_{ex}	0.5 0.7 1.0
	Die angle	2α	90°
	Tool radius	r_{ex}	3 mm
	Die land	l_{ex}	2.5 mm
b)	Area reduction	ε_{bc}	0.2 0.4 0.6
	Tool radius	r_{bc}	3 mm
	Punch land	l_{bc}	2.5 mm
c)	Extrusion strain	ε_{ex}	0.5
	Die angle	2α	60°
	Tool radius	r_{ex}	3 mm
	Undercut inclination	2β	40°
d)	Area reduction	ε_{ex}	0.4
	Tool radius	r_{ex}	3 mm
	Flange diameter	d_f	36 mm

$$f(\boldsymbol{\sigma}, \bar{\boldsymbol{\varepsilon}}) = \sigma_{Mises}(\boldsymbol{\sigma}) - \sigma_{f,iso}(\bar{\boldsymbol{\varepsilon}}) = 0 \tag{12}$$

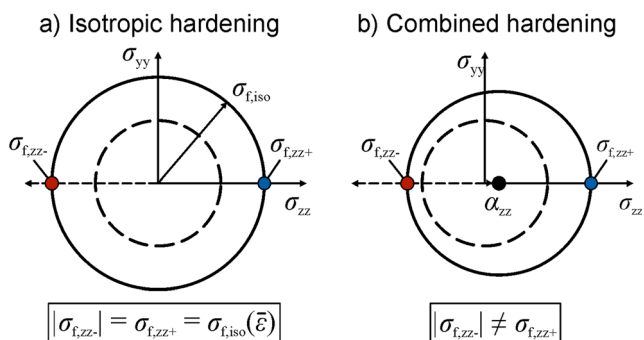


Fig. 15 Flow stress under uniaxial loading in z-direction for (a) isotropic hardening, (b) combined hardening

and can thus be determined explicitly as a function of the local equivalent plastic strain $\bar{\boldsymbol{\varepsilon}}$. In this case, the flow stress is independent of the sign of the load (Fig. 15a).

For combined isotropic-kinematic hardening models, the local flow stress is determined via the altered yield condition:

$$f(\boldsymbol{\sigma}, \boldsymbol{\alpha}, \boldsymbol{\varepsilon}) = \sigma_{Mises}(\boldsymbol{\sigma} - \boldsymbol{\alpha}) - \sigma_{f,iso}(\boldsymbol{\varepsilon}) = 0. \tag{13}$$

The back stress tensor $\boldsymbol{\alpha}$ leads Eq. 13 to have two different solutions for any fixed load direction, corresponding to the flow stress under uniaxial tensile loading $\sigma_{f,zz+}$ and the flow stress under uniaxial compressive loading $\sigma_{f,zz-}$ (Fig. 15b).

The local flow stress distribution of a forward extruded component under the assumption of uniaxial loading in z-direction is illustrated in Fig. 16 considering isotropic and anisotropic hardening (modified Yoshida-Uemori). During uniaxial compression, the kinematic hardening models predict a flow stress $\sigma_{f,zz-}$ that is significantly lower compared to the flow stress under uniaxial tension $\sigma_{f,zz+}$. Interestingly, in the region close to the surface even the tensile flow stress is lower as compared to the isotropic hardening model, giving a first hint on the existence of an intrinsic strain path reversal.

The local Bauschinger coefficient describes the ratio between the flow stress under tension and compression for a fixed uniaxial stress state. The Bauschinger coefficient assuming tensile and compressive loading under a uniaxial loading in z-direction is thus given by

$$\chi_{zz} = \frac{|\sigma_{f,zz-}|}{\sigma_{f,zz+}}. \tag{15}$$

The influence of the extrusion strain on the distribution of the local Bauschinger coefficient in forward extruded rods is shown in Fig. 17.

The evolution of the Bauschinger coefficient highlights the existence of intrinsic strain path changes. These strain path changes are especially pronounced for material points traveling

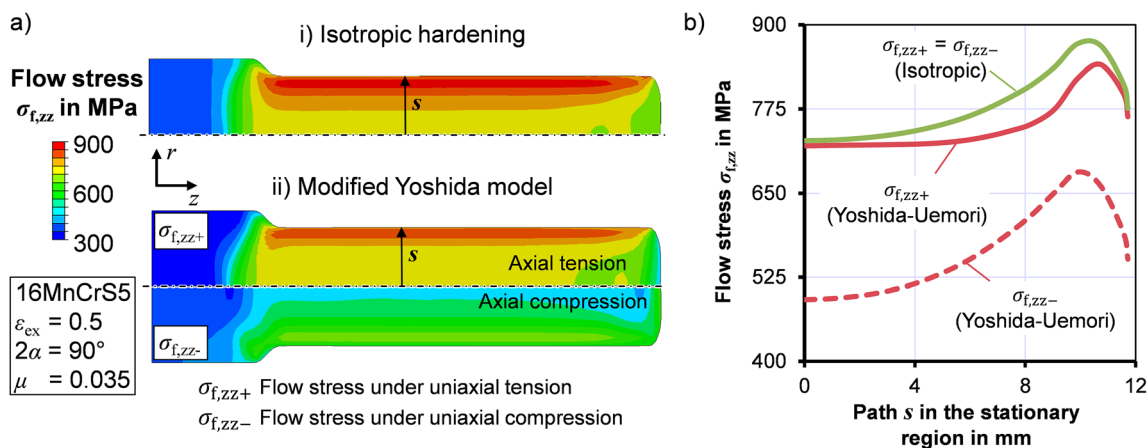


Fig. 16 a Local flow stress distribution after forward rod extrusion predicted by (i) isotropic and (ii) anisotropic hardening models, b Flow stress distributions over the radius of the extrudates

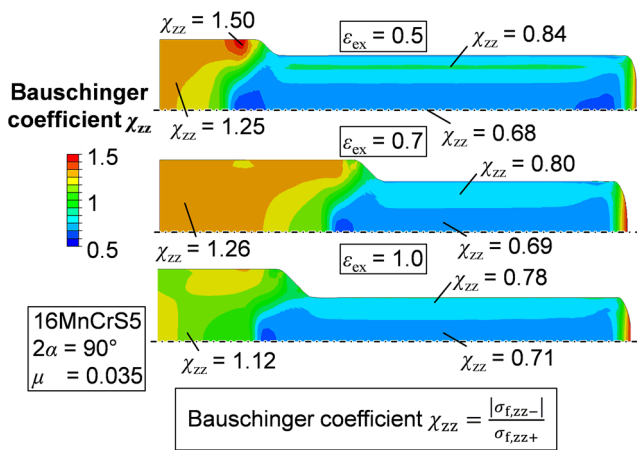


Fig. 17 Influence of extrusion strain on the local Bauschinger coefficients considering uniaxial loading in z-direction

along surface-near particle lines. For example, for $\epsilon_{ex} = 0.5$, a particle moving along surface-near particle line experiences a maximum Bauschinger coefficient of $\chi_{zz} = 1.5$ and ends up with a coefficient of $\chi_{zz} = 0.84$, which means that it is first compressed significantly before flowing into the die opening and then stretched. In the core of the extruded rods, the Bauschinger coefficients end up in the range of $0.68 < \chi < 0.71$, which coincides well with the experimentally obtained Bauschinger coefficients ($\chi_{zz, exp} = 0.67$), since the data was used as the basis for the parameter identification procedure. All investigated kinematic hardening models are capable to model the experimentally observed flow stress difference considering tension and compression after forward rod extrusion. The conventional assumption of isotropic hardening leads to errors in the local flow stress prediction of up to 32% ($\epsilon_{ex} = 0.5$).

Figure 18a shows the calculated flow stress distribution in a backward extruded can (20% area reduction), assuming isotropic and kinematic hardening. In analogy to forward rod extrusion, in the formed region the flow stress during uniaxial tension is higher than during uniaxial compression, as the material is predominantly stretched in axial direction. The influence of the area-reduction on the local Bauschinger effect

is shown in Fig. 18b. Regardless of the area-reduction, the kinematic hardening model predicts a local Bauschinger coefficient above 1 below the punch and a value below 1 in the can wall. Again, this highlights the existence of an intrinsic strain path strain path reversal, which is expected to have an impact on secondary part properties like residual stresses as well as the process forces. Regardless of the area-reduction, the kinematic hardening model predicts a local Bauschinger coefficient larger than 1 below the punch, where the material is compressed and a value lower than 1 in the can region. Again, the consequence is that some material regions undergo a significant intrinsic strain path change, which is expected to have an impact on secondary part properties like residual stresses as well as the process forces.

Influence of anisotropic hardening on residual stresses

To investigate the influence of anisotropic hardening on the residual stresses, the evolution of the axial stress in the core of the extrudate during ejection after forward rod extrusion is shown in Fig. 19a. To correctly simulate the springback of the container and die after unloading, which is important for the correct calculation of residual stresses in the workpiece, the dies were simulated as elastic objects as described in Appendix A.1.

During the ejection process, the extrudate can be subdivided into three individual sections: Section ① is the head region, which has only been axially compressed. As the material in the surface region is compressed more than the material in the core, the inhomogeneity of axial elastic springback after unloading leads to tensile residual stresses in the core of the head region. As the amount of elastic springback is not affected by anisotropic hardening in this region, all constitutive models predict the same axial stress.

During ejection, Section ② is actively compressed between the ejector and the friction surfaces in the die cavity and the head, leading to overall compressive stresses in the core of the shaft. In this region, the combined work-hardening models predict lower

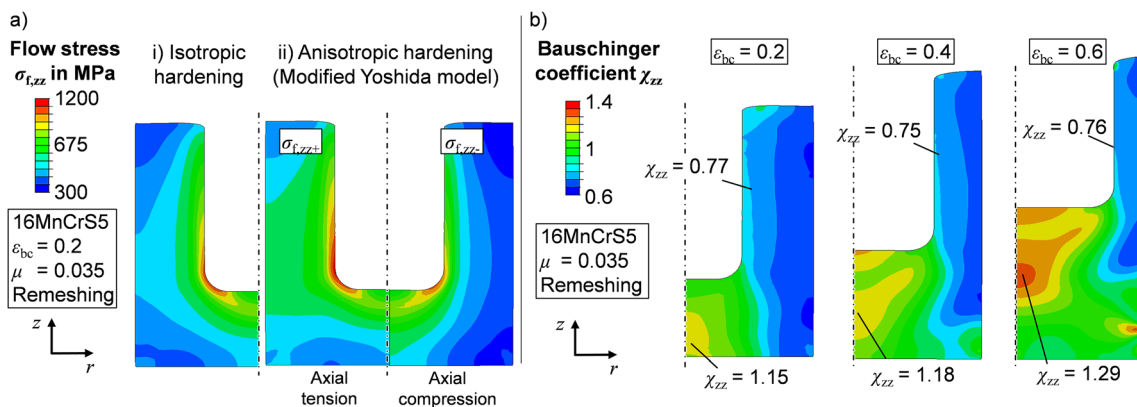


Fig. 18 **a** Local flow stress distribution after backward can extrusion calculated by isotropic and anisotropic hardening models, **b** Influence of area-reduction on the resulting local Bauschinger coefficients considering uniaxial loading in z-direction

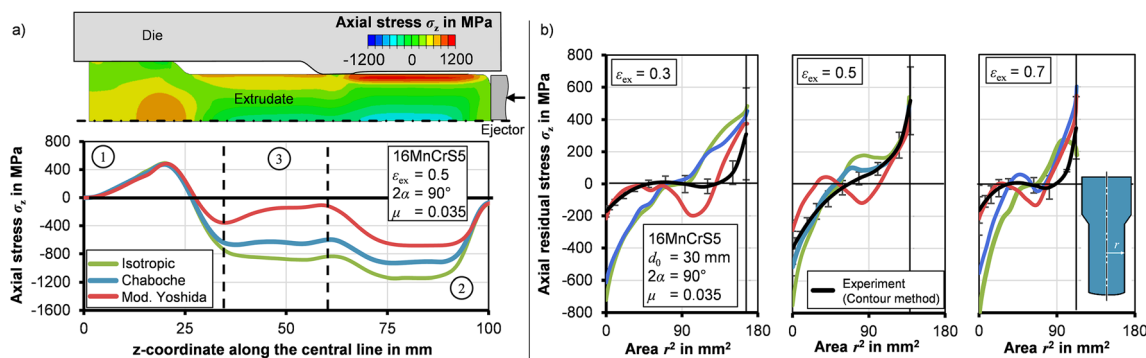


Fig. 19 **a** Axial stress evolution along the extrudate core in forward rod extrusion during ejection, **b** Influence of the extrusion strain on the axial residual stress distribution over the squared radius of the formed shaft after forward rod extrusion

axial stresses than the conventional isotropic hardening model. The reduced stresses are the consequence of a lowered elastic strain inhomogeneity over the shaft radius, which is caused by the intrinsic strain path change during forward extrusion. As the surface near material is subject to a more significant strain path change than the material in the core, the work-hardening in the surface region is reduced in the case of the anisotropic hardening models. The reduced work-hardening leads to a reduction of the elastic strain inhomogeneity over the radius, which results in lowered residual stresses. The effect is most pronounced for the modified Yoshida-Uemori model, which is also able to capture the work-hardening stagnation, triggered during the intrinsic strain path change in the surface-near material. The work-hardening stagnation leads to an even more pronounced reduction of the work-hardening inhomogeneity over the radius, and thus to a reduction of the elastic strain inhomogeneity. Lastly, in Section ③ new plastic strains caused by the ejection process lead to another reduction of the elastic strain inhomogeneity and thus to an additional reduction of the axial stress. In the case of the anisotropic hardening models, this axial stress relaxation is more pronounced due the overall lowered flow stress under compression, as compared to the isotropic hardening models, manifesting in a more pronounced plasticization over the cross-section.

Figure 19b shows the axial residual stress distribution in completely unloaded forward extruded shafts for different constitute models and extrusion strains over the (squared) radius. Again, all anisotropic hardening models predict lower residual stresses than the isotropic hardening model. Among these, the modified Yoshida-Uemori model predicts the lowest residual stresses. In addition to the numerical results, the axial residual stresses were determined experimentally using the contour method introduced by Prime [44]. Details regarding the application of this method for forward extruded rods are given in Appendix A.2. The experimental results suggest, that the isotropic hardening model as well as the Chaboche model, overestimate the residual stresses significantly, especially in the core of the extrudate. For the investigated extrusion strains, the modified Yoshida-Uemori model shows the best correlation with the experiments. The deviation at $80 \text{ mm}^2 < r^2 < 95 \text{ mm}^2$ is assumed to be related to inaccuracies of the contour method which is not able to capture abrupt changes of the residual stress distribution.

The lowered residual stresses predicted by the anisotropic hardening models can be explained by a thought experiment adapted from Tekkaya and Gerhardt [45] (Fig. 20). A cylindrical specimen is considered, which is subject to a similar axial residual stress distribution as a forward extruded shaft before ejection

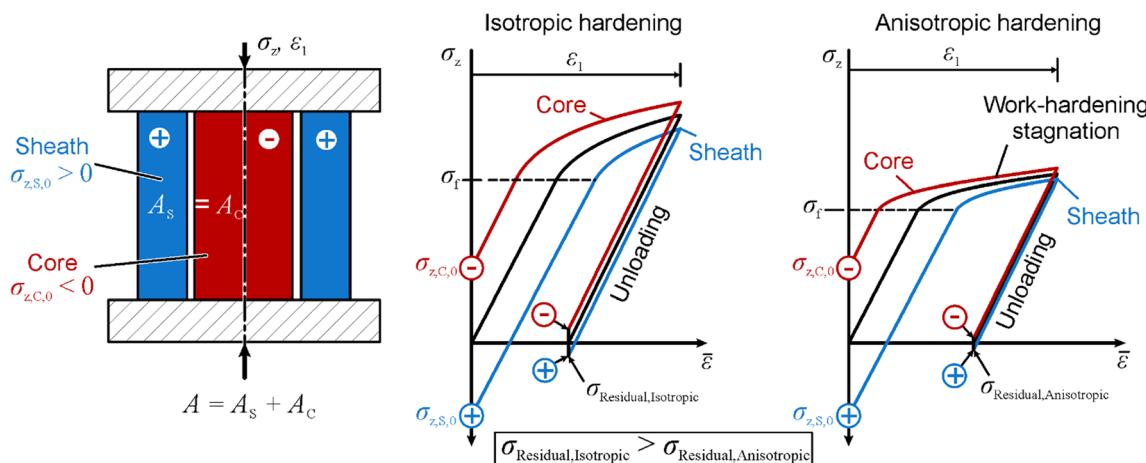


Fig. 20 Thought experiment to explain the residual stress relaxation during ejection after forward rod extrusion, considering isotropic and anisotropic work-hardening (inspired by Tekkaya et al. [45]; y-axes are flipped)

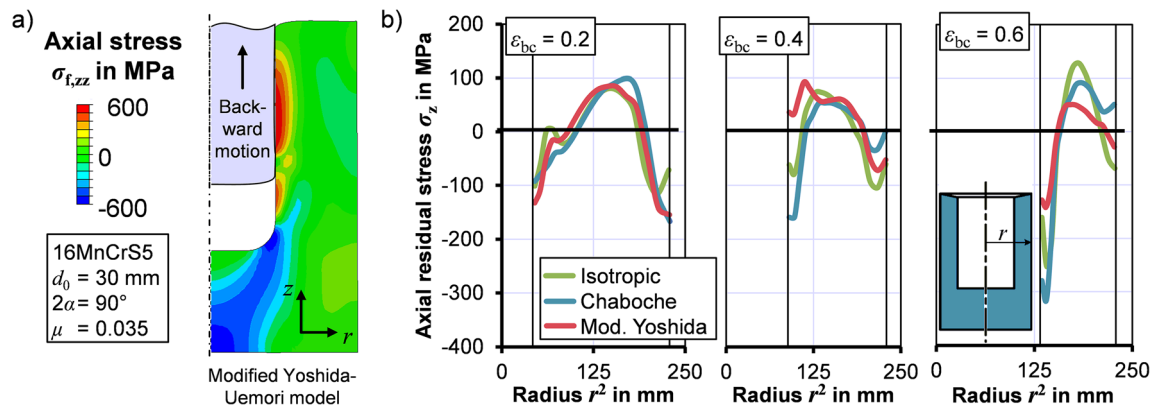


Fig. 21 **a** Evolution of axial stress during the punch backward motion in backward can extrusion (container is hidden for improved illustration), **b** Axial residual stress over the cup wall for different area reductions as predicted by the different hardening models

(compressive residual stress $\sigma_{z,C,0} < 0$ in the core over the area A_C and tensile residual stress $\sigma_{z,S,0} > 0$ in the sheath over the area A_S). If the specimen is loaded with a compression stress of σ_z (in analogy to the compressive stress caused by the ejector), the loading stresses are added up on the residual stresses. In this case, the core will plastically deform first and work-harden. When the sheath starts plastically deforming as well, the flow stress in the core and sheath approach each other. If the specimen is then unloaded, the elastic strain inhomogeneity is reduced which leads to the residual stress relaxation. In the original thought experiment, the dominant loading stress during ejection was assumed to be tensile, which is true for isotropic materials as the relaxation of the die cavity leads to a second extrusion process. However, due to the lower flow stress of the previously extruded (elongated) material during subsequent compression, the material is predominantly compressed axially before flowing into the reduced die cavity. Based on these observations, the y-axes in Fig. 20 were flipped. In addition to this, anisotropic hardening includes work-hardening stagnation, which accelerates the approach of the flow curves in the core and the sheath region, leading to an intensification of the residual stress relaxation.

To conclude the residual stress investigations, the axial stress evolution during the punch backward motion after backward can extrusion is shown in Fig. 21a. Analogously to forward rod extrusion, the elastic springback of the container and the springback of the workpiece after unloading, lead to a second

forming stage during the punch backward motion. The numerically determined axial residual stress within backward extruded cans after ejection is shown for three area reductions ε_{bc} (Fig. 21b). At the lowest investigated area reduction ($\varepsilon_{bc} = 0.2$), there exists only a small deviation between the individual constitutive models. With increasing area reduction, however, the axial residual stress distributions predicted by the models drift apart. In analogy to forward rod extrusion, the modified Yoshida-Uemori model predicts the lowest axial residual stresses, as the work-hardening stagnation occurring after the initial upsetting of the workpiece in the container and the subsequent axial elongation leads to a reduction of the axial strain inhomogeneity over the thickness of the can wall.

Influence of anisotropic hardening on process forces

Figure 22a shows the punch force F over the stroke s in forward rod extrusion calculated by the isotropic and anisotropic hardening models along with the corresponding experimental measurements (dashed lines). While all numerically determined force-stroke-curves are in good correlation with the experimentally obtained data, the results suggest that anisotropic hardening does not have a significant effect on the punch force in single-stage forging processes. The effects of the intrinsic strain path changes demonstrated in the previous sections even out over the forming zone. The influence of anisotropic hardening on the ejector force

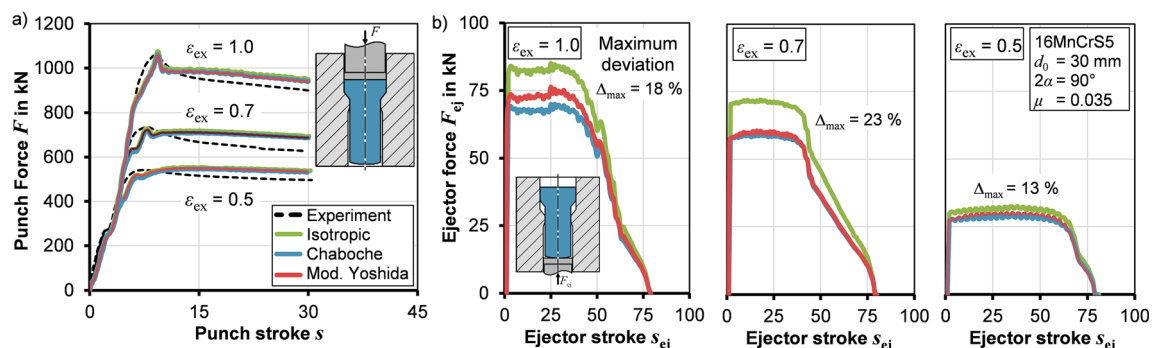


Fig. 22 Influence of anisotropic hardening on (a) punch forces and (b) ejector forces in forward rod extrusion

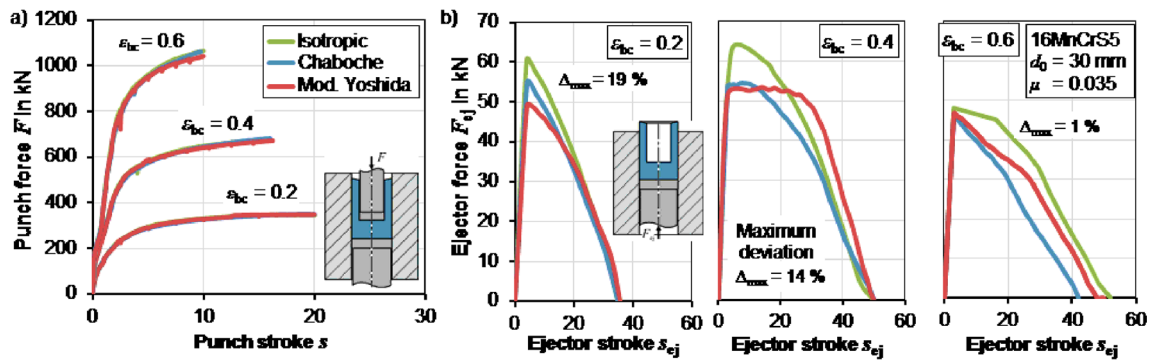


Fig. 23 Influence of anisotropic hardening on (a) punch forces and (b) ejector forces in backward can extrusion

F_{ej} after forward rod extrusion is shown in Fig. 22b. The reduced flow stress under the compressive stresses present during the ejection process, leads to an overall reduction of the predicted ejector force for all extrusion strains. The experimental setup did not allow for measurements of the ejector forces for validation, which will be repeated in future investigations.

The forming and ejector forces in backward can extrusion predicted by the isotropic and anisotropic hardening models are shown in Fig. 23. In analogy to forward rod extrusion, the forming forces in backward can extrusion are only weakly affected by anisotropic hardening. However, the strain path change caused by the load reversal during ejection leads to a reduction of the ejector forces as new plastic strains generated during ejection occur under a lower flow stress as compared to isotropic hardening. For the area reduction of $\epsilon_{bc} = 0.2$ the difference between isotropic hardening and the modified Yoshida-Uemori model amounts to 19%.

Lastly, the effect of anisotropic hardening on the forming forces in multi-stage forming processes is shown by the examples of anchor forging after forward rod extrusion (Fig. 24a) and flange forging after backward can extrusion (Fig. 24b). In both process sequences, the material is subjected to a complete strain path reversal. The average deviation between the force-stroke curves calculated considering isotropic and anisotropic hardening amounts to 11%, whereas the highest deviations are in the range of 12% to 19%. The deviation of the forming forces correlates with the permanent softening of 16MnCrS5 (see Fig. 11). For materials with a more pronounced permanent softening or even a complete loss of the work-hardening tendency after strain path

reversal (see C15), the influence of anisotropic hardening on the forming forces is expected to be even more significant.

Conclusions

The result of this investigation contribute to the three fields (i) characterization, (ii) constitutive modelling and (iii) implications for bulk metal forming in the context of strain path reversals.

(i) *Characterization of large strain anisotropic hardening:*

- Tensile and compression tests on forward extruded material reveal the large strain anisotropic work-hardening behaviour of 16MnCrS5, C15 and 100Cr6 up to equivalent strains of 1.7 and accumulated strains of 2.5.
- All investigated steels exhibit near linear work-hardening for monotonic deformation for strains above 1.0.
- All steels exhibit the Bauschinger effect, transient hardening, work-hardening stagnation and permanent softening, all of which intensify with the pre-strain. In the extreme case of C15, no more work-hardening is observed after pre-strains above 0.5.

(ii) *Modelling of large strain anisotropic hardening:*

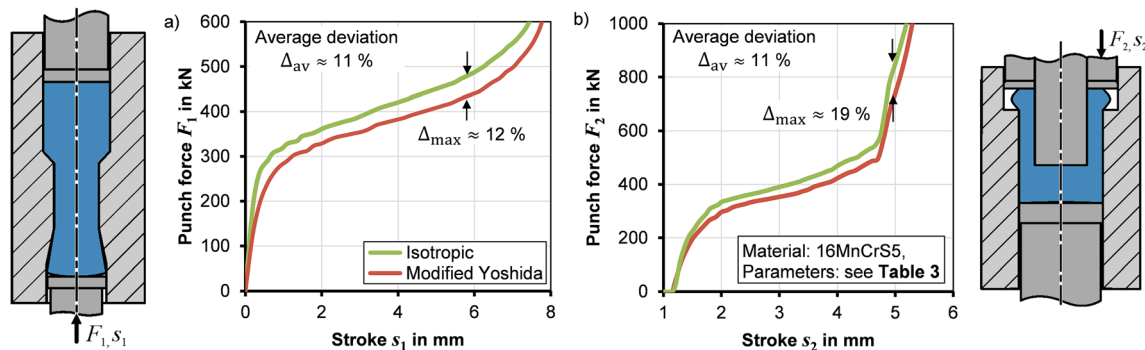


Fig. 24 Effect of anisotropic hardening on the punch forces in multi-staged forming: (a) Anchor forging, (b) Flange forging

- The consideration of isotropic hardening leads to a significant overestimation of the materials' flow stress after a strain path reversal ($15\% < \Delta\bar{\sigma}_f < 50\%$)
- A modified version of the Yoshida-Uemori model was implemented. The modifications were necessary to successfully capture the experimentally observed large strain anisotropic work-hardening phenomena exhibited by the case-hardening steel 16MnCrS5 over the complete relevant equivalent strain and pre-strain regimes. The modifications include the generalization of the isotropic hardening relation to model the linear work-hardening under monotonic loading and the split of the rates of isotropic and kinematic hardening of the bounding surface.

(iii) *Consequences of anisotropic hardening in cold forging:*

- The altered flow stress distribution leads to a significant reduction of the forming-induced residual stresses due to intrinsic strain path changes and strain path changes during component ejection.
- While the punch force is only weakly affected by anisotropic hardening in single-stage forming processes (the difference between isotropic hardening and the modified Yoshida-Uemori model is less than 5%), the ejector forces are affected significantly (up to 19%).
- For multi-stage forming processes, in which relevant material regions are subjected to a strain path reversal, anisotropic hardening causes a reduction of the forming force is compared to isotropic hardening (difference between isotropic hardening and modified Yoshida-Uemori model $11\% < \Delta\bar{F} < 19\%$).

Further experimental investigations on the influence of strain path changes will focus on the influence of cross-hardening effects. To characterize materials accordingly, the procedure of tensile tests on cold forward extruded material utilized in this work can be modified by extraction of torsion test specimens from the uniformly deformed region. The subsequent torsion loading corresponds to an orthogonal strain path change, which should reveal potential cross-hardening effects. In addition, the influence of the temperature and strain rate on the large strain anisotropic work-hardening will be evaluated by conducting experiments at elevated temperatures and strain rates (according to “Large strain monotonic work-hardening behaviour” section).

Appendix

Numerical simulation of cold forging processes

The FEM program Abaqus CAE 2019 was used for the conduction of the numerical investigations. The model setup of

forward rod extrusion at different process stages is shown in Appendix Fig. 25.

For all cold forging processes, the workpiece was modelled as an elastic-plastic object assuming isotropic linear elasticity with constant elastic parameters and the described plasticity models. To correctly simulate the residual stress reduction during part ejection, according to Tekkaya [45], the dies were simulated as an elastic object with a Young's modulus of $E_{\text{die}} = 210 \text{ GPa}$ and a Poisson's ratio $\nu_{\text{die}} = 0.3$. The flow curve of 16MnCrS5 was determined by means of the experimental procedure presented in “Large strain monotonic work-hardening behaviour” section. The effect of the temperature increase ΔT during cold forging on the current flow stress was neglected due to its minor influence on the resulting local workpiece properties after forming ($\Delta T < 250 \text{ }^\circ\text{C}$ for $\varepsilon_{\text{ex}} = 1.5$, see “Large strain monotonic work-hardening behaviour” section).

The workpiece was meshed with 2D-axisymmetric 4-node quadrilateral elements with reduced integration (CAX4R). To determine a suitable mesh size, a mesh convergence study, was conducted. As the calculated residual stresses are the physical quantity most sensitive with respect to the mesh quality, they were used as the target quantity in the mesh convergence study. The number of elements was determined by the example of forward rod extrusion ($\varepsilon_{\text{ex}} = 0.7$, $2\alpha = 90^\circ$, $r_{\text{ex}} = 3 \text{ mm}$, $\mu = 0.04$). The results of the mesh convergence study are shown in Appendix Fig. 26.

The punch force converges at 2000 elements, the strain and residual stress converge at 7500 elements. As the calculation time increases from 20 min to about 200 min between the two settings, the solution with the lower number of elements was considered to be sufficiently accurate. The mesh density of 7 elements/ mm^2 was applied for all simulations. The dies were meshed with 4800 elements each. The die mesh was refined at

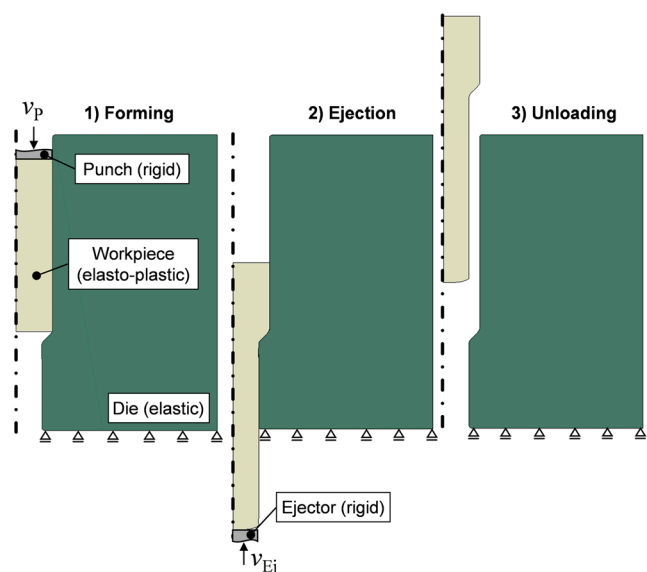
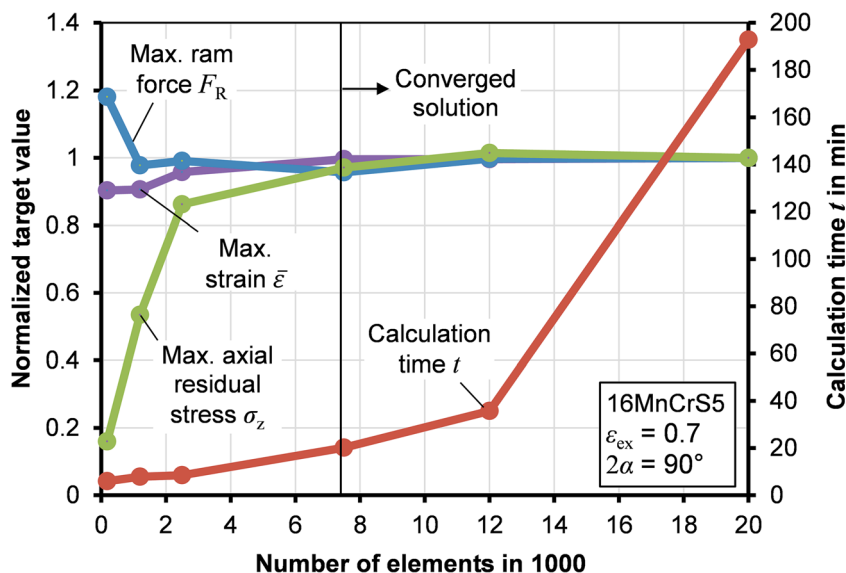


Fig. 25 Simulated process stages in forward rod extrusion

Fig. 26 Effect of the element number on the maximum ram force, maximum strain and maximum axial residual stress



the die shoulders, as this is the location of maximum elastic deflection. The node-to-surface contact algorithm was utilized to model the contact between the dies and the workpiece. To simulate the friction between the workpiece and the die, the Coulomb friction model was used. The constant friction coefficient of $\mu < 0.035$ was determined iteratively to acquire the best possible fit between simulated and the experimentally obtained ram forces for all investigated extrusion ratios.

1. Cutting of the parts cross-sections by wire-electronic discharge machining
2. Contour measurement of the cut surfaces
3. Application of the contour plot of the cut surfaces as reverse displacement field in numerical simulations of the ideally cut geometry
4. Post-processing of the resulting normal stresses at the surface which equal the residual stresses normal to the cutting plane before cutting

Residual stress measurement via contour method

The contour method by Prime [44] was used to determine the axial residual stress distribution of forward extruded rods. The basic process principle of the contour method is visualized in Appendix Fig. 27a. To determine the axial residual stress distribution of forward extruded parts, the following steps are conducted:

The extrudates were clamped with a special clamping device, which allows exact positioning of the extrudate during wire cutting (Appendix Fig. 28).

The wire diameter was chosen 0.25 mm and the wire tension was set to 12 N. The extrudates were cut at a speed of 3.84 mm min^{-1} . The flushing nozzle pressure was set to 12 bar. The resulting roughness of the cut surfaces was $R_a = 2.8 \text{ }\mu\text{m}$. The contour of the cut surfaces was measured using a tactile coordinate

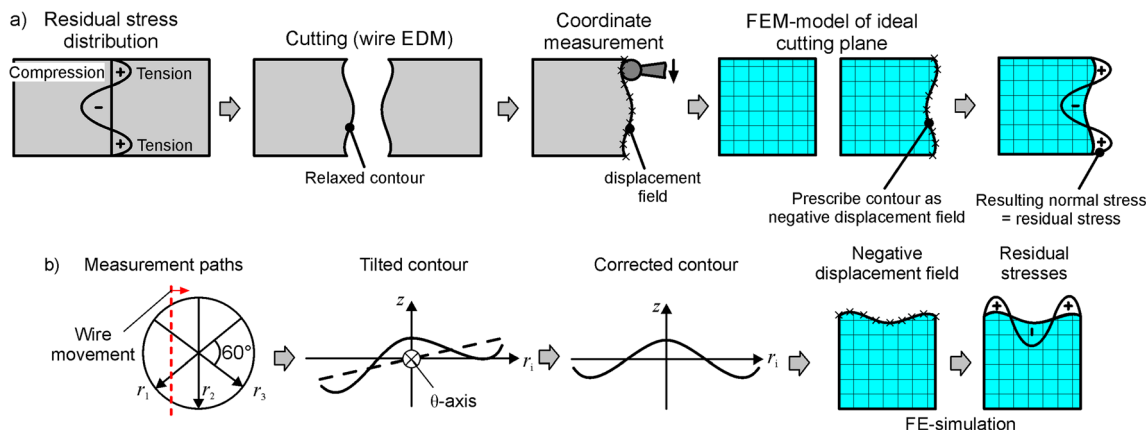
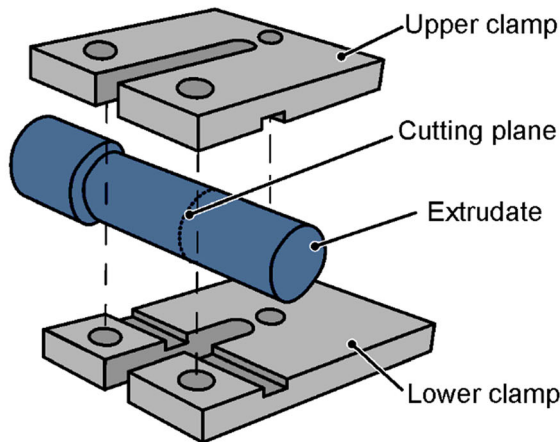


Fig. 27 a Basic principle of the contour method to determine residual stresses as described by Prime [44]. b Post-processing of the contour data to obtain the residual stress distribution normal to the cutting plane

a) Clamping setup



b) Wire-cut EDM

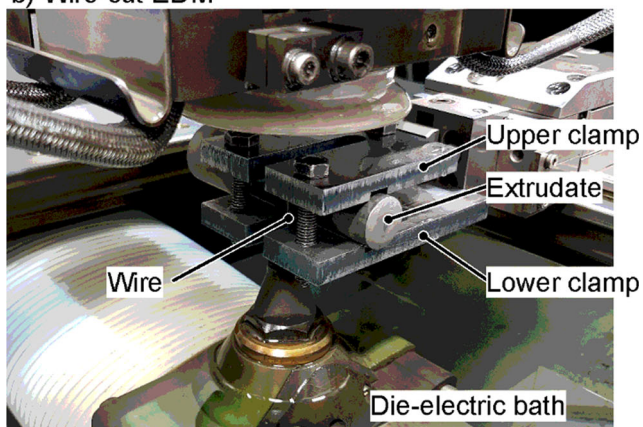


Fig. 28 Wire-cutting setup

measurement system Zeiss PRISMO VAST 5 HTG with a resolution of 1 μm . The extrudate halves were measured along three linear radial paths orientated at angles of 60° each, making up a total of six contour paths per extrudate. The measured data was post-processed according to Appendix Fig. 27b.

Each measured contour was rotated around the θ -axis to and compensate tilting with respect to the z -axis. The contours are approximated by a polynomial of sixth degree to smooth the data scattering caused by the surface roughness. Finally, the processed contour data of each extrudate is applied to an idealized FEM-model of the cut extrudate in terms of a negative displacement field. The simulations were set-up as axisymmetric FEM-models in Abaqus Standard. The material behaviour was assumed elastic with a Young's modulus of $E = 210.000 \text{ MPa}$ and a Poisson's ratio of $\nu = 0.3$, assuming that the wire-cutting process leads to purely elastic unloading. The resulting normal stress distributions on the cutting plane equal the forming-induced residual stress field pre-sent in the extrudate before wire-cutting.

The results for parts with three extrusion strains are shown in Appendix Fig. 29. The error bars indicate the standard deviation of six contour measurements per extrusion strain.

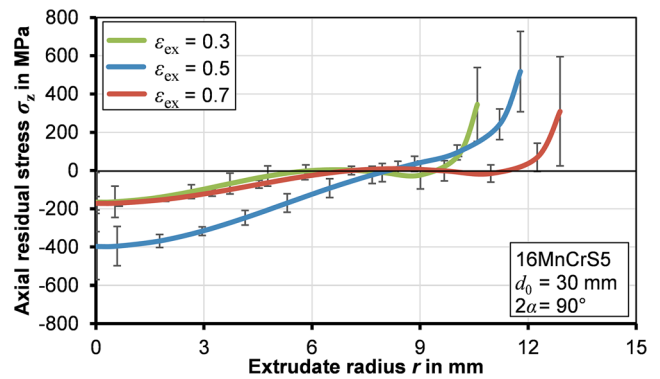


Fig. 29 Axial residual stress distribution in the shaft of forward extruded parts for three different extrusion ratios as obtained by the contour method

In the core of the extrudates, there exists a compressive residual stress, whereas, towards the surfaces the material is subject to positive residual stress. Qualitatively, the results of the contour method match well with the expected axial residual stress distributions.

Acknowledgements The authors thank the German Research Foundation (DFG) for the financial support of the project “Influence of the Multiaxial Bauschinger Effect in Cold Forging” (project number 418815343). Also we would like to thank Dr.-Ing. Till Clausmeyer for his valuable comments on the initial manuscript.

Funding Open Access funding enabled and organized by Projekt DEAL. The authors acknowledge funding from the German Research Foundation (DFG) for the project “Influence of the Multiaxial Bauschinger Effect in Cold Forging” (project number 418815343).

Declarations

Conflict on interests The authors declare that they have no conflict of interest.

Open Access This article is licensed under a Creative Commons Attribution 4.0 International License, which permits use, sharing, adaptation, distribution and reproduction in any medium or format, as long as you give appropriate credit to the original author(s) and the source, provide a link to the Creative Commons licence, and indicate if changes were made. The images or other third party material in this article are included in the article's Creative Commons licence, unless indicated otherwise in a credit line to the material. If material is not included in the article's Creative Commons licence and your intended use is not permitted by statutory regulation or exceeds the permitted use, you will need to obtain permission directly from the copyright holder. To view a copy of this licence, visit <http://creativecommons.org/licenses/by/4.0/>.

References

1. Tekkaya AE, Allwood JM, Bariani PF, Bruschi S, Cao J, Gramlich S, Groche P, Hirt G, Ishikawa T, Löbke C, Lueg-Althoff J, Merklein M, Misiolek WZ, Pietrzyk M, Shivpuri R, Yanagimoto J (2015) Metal forming beyond shaping: predicting and setting product properties. CIRP Ann 64:629–653

2. Tekkaya AE, Bouchard P-O, Bruschi S, Tasan CC (2020) Damage in metal forming. *CIRP Ann* 69(2):600–623
3. Bauschinger J (1886) Über die Veränderung der Elastizitätsgrenze und die Festigkeit des Eisens und Stahls durch Strecken und Quetschen, durch Erwärmen und Ab-kühlen und durch oftmals wiederholte Beanspruchungen. Mittheilungen aus dem Mechanisch-Technischem Laboratorium
4. Masing G (1923) Zur Heynschen Theorie der Verfestigung der Metalle durch verborgene elastische Spannungen. In: Harries CD (ed) *Wissenschaftliche Veröffentlichungen aus dem Siemens-Konzern*, III. Band, vol 3. Springer, Berlin
5. Orowan E (1959) Causes and effects of internal stresses. In: Rassweiler GM, Grube WL (eds) *Internal stresses and fatigue in metals, Causes and effects of internal stresses*. Elsevier, New York, p 71
6. Sleswyk AW, Kassner ME, Kemerink GJ (1986) The effect of partial reversibility of dislocation motion. In: Gittus J, Zarka J, Nemat-Nasser S (eds) *Large deformations of solids: physical basis and mathematical modelling*. Springer, Dordrecht, pp 81–98
7. Sillekens WH, Dautzenberg JH, Kals JAG (1988) Flow curves for C45 steel at abrupt changes in the strain path. *CIRP Ann* 37:213–216
8. Hasegawa T, Yakou T, Karashima S (1975) Deformation behavior and dislocation structure upon stress reversal in polycrystalline Aluminium. *Mater Sci Eng* 20:267–276
9. Edwards EH, Washburn J (1954) Strain hardening of latent slip systems in zinc crystals. *JOM* 6:1239–1242
10. Sowerby R, Uko DK, Tomita Y (1979) A review of certain aspects of the Bauschinger effect in metals. *Mater Sci Eng* 41(1):43–58
11. Scholtes B, Voehringer O, Macherauch E, (1980) Die Auswirkung des Bauschingerereffekts auf das Verformungsverhalten technisch wichtiger Vielkristalle. *Steel Research*
12. Yoshida F, Uemori T, Fujiwara K (2002) Elastic–plastic behavior of steel sheets under in-plane cyclic tension–compression at large strain. *Int J Plast* 18(5-6):633–659
13. Ghaei A, Green DE (2010) Numerical implementation of Yoshida–Uemori two-surface plasticity model using a fully implicit integration scheme. *Comput Mater Sci* 48(1):195–205
14. Wagoner RH, Lim H, Lee M-G (2013) Advanced issues in springback. *Int J Plast* 45:3–20
15. Abel A, Ham RK (1966) The cyclic strain behaviour of crystals of aluminum-4 wt.% copper-i. the bauschinger effect. *Acta Metall* 14(11):1489–1494
16. Tan Z, Magnusson C, Persson B (1994) The Bauschinger effect in compression-tension of sheet metals. *Mater Sci Eng A* 183(1-2):31–38
17. Kuwabara T, Nagata K, Nakako T (2001) Measurement and analysis of the Bauschinger effect of sheet metals subjected to in-plane stress reversals. *International conference of advanced materials and processing technology*, pp. 407–414
18. Boger RK (2006) *Non-monotonic strain hardening and its constitutive representation*. Ohio State University, Materials Science and Engineering. Dissertation
19. Hu Z, Rauch EF, Teodosiu C (1992) Work-hardening behavior of mild steel under stress reversal at large strains. *Int J Plast* 8(7):839–856
20. Yoshida F, Urabe M, Toropov VV (1998) Identification of material parameters in constitutive model for sheet metals from cyclic bending tests. *Int J Mech Sci* 40(2-3):237–249
21. Yin Q, Tekkaya AE, Traphöner H (2015) Determining cyclic flow curves using the in-plane torsion test. *CIRP Ann* 64(1):261–264
22. Tozawa Y, Kojima M (1971) Effect of pre-deformation process on limit and resistance in upsetting deformation. *J Jpn Soc TechnolPlast* 12:174–182
23. Havranek J (1984) The effect of pre-drawing on strength and ductility in cold forging. *Adv Technol Plast* 2:845–850
24. Ma L (2007) Effect of pre-drawing on formability during cold heading. Library and Archives Canada, Ottawa
25. Miki T, Toda M (1988) Evaluation of work hardening and Bauschinger effect of steels under cold forging by the half-value breadth of X-ray diffraction profile. *J Soc Mater Sci Jpn* 38:398–403
26. Galdos L, Agirre J, Mendiguren J, Argandona E.S de, Otegi N, Trinidad J (2019a) Mixed isotropic–kinematic hardening model for cold forging simulation of an industrial bolt. *Proceedings of the 52nd ICFG plenary meeting*
27. Galdos L, Agirre J, Otegi N, Mendiguren J, Argandona ES de (2019b) Hardening characterization of cold forging steel by means of compression and torsion tests. 8th manufacturing engineering society international conference
28. Sillekens WH, Dautzenberg JH, Kals JAG (1991) Strain path dependence of flow curves. *CIRP Ann* 40:255–258
29. Langford G, Cohen M (1969) Strain hardening of Iron by severe plastic deformation. *Trans ASM* 62:623–638
30. Pöhlandt K (1979) Beitrag zur Aufnahme von Fließkurven bei hohen Umformgraden. Seminar "Neuere Entwicklungen in der Massivumformung". Forschungsgesellschaft Umformtechnik mbH, Stuttgart
31. Doege E, Meyer-Nolkemper H, Saeed I (1986) Fließkurvenatlas metallischer Werkstoffe. Mit Fließkurven für 73 Werkstoffe und einer grundlegenden Einführung. Hanser, München
32. Nehl E (1983) Untersuchungen zum Halbwarmfließpressen von Automatenstählen. Springer, Berlin
33. Chaboche JL (1986) Time-independent constitutive theories for cyclic plasticity. *Int J Plast* 2(2):149–188
34. Barlat F, Gracio JJ, Lee M-G, Rauch EF, Vincze G (2011) An alternative to kinematic hardening in classical plasticity. *Int J Plast* 27(9):1309–1327
35. Suh YS, Agah-Tehrani A, Chung K (1991) Stress analysis of axisymmetric extrusion in the presence of strain-induced anisotropy modeled as combined isotropic-kinematic hardening. *Comput Methods Appl Mech Eng* 93:127–150
36. Narita S, Uemori T, Hayakawa K, Kubota Yoshihiro, K. (2016) Effect of Hardening Rule on Analysis of Forming and Strength of Multistage Cold Forged Bolt without Heat Treatment. *Journal of the Japan Society for Technology of Plasticity* 57(670):1070–1076
37. Hering O, Kolpak F, Tekkaya AE (2019) Flow curves up to high strains considering load reversal and damage. *Int J Mater Form* 12(6):955–972
38. Siebel E (1956) Die Bedeutung der Fließkurve bei der Kaltumformung. *VDI-Z* 98:133–134
39. Yoshida F, Uemori T (2002) A model of large-strain cyclic plasticity describing the Bauschinger effect and workhardening stagnation. *Int J Plast* 18(5-6):661–686
40. Yoshida F, Hamasaki H, Uemori T (2013) Modeling of anisotropic hardening of sheet metals. *AIP Conf Proc* 1567:482–487
41. Swift HW (1952) Plastic instability under plane stress. *J Mech Phys Solids* 1(1):1–18
42. Voce E (1948) The relationship between stress and strain for homogeneous deformation. *J Inst Met* 74:537–562
43. Stander N, Craig KJ, Müllerschön H, Reichert R (2005) Material identification in structural optimization using response surfaces. *Struct Multidiscip Optim* 29(2):93–102
44. Prime MB (2000) Cross-sectional mapping of residual stresses by measuring the surface contour after a cut. *J Eng Mater Technol* 123: 162–168
45. Tekkaya AE, Gerhardt J, Burgdorf M (1985) Residual stresses in cold-formed workpieces. *CIRP Ann* 34:225–230